



Experimental Implementation of Modal Approaches for Reattachment of Separated Flows

Eric Deem*, Louis Cattafesta[†]

Mechanical Engineering, Florida State University, Tallahassee, FL, 32310

Huaijin Yao[‡], Maziar Hemati[§]

Aerospace Engineering and Mechanics, University of Minnesota, Minneapolis, MN, 55455

Hao Zhang[¶], Clarence Rowley^{||}

Mechanical and Aerospace Engineering, Princeton University, Princeton, NJ, 08544

Methods for adaptive control of flow separation based on dynamic mode decomposition (DMD) are formulated and implemented on a canonical separated flow subjected to actuation by a zero-net mass-flux (ZNMF) jet actuator. Using a linear array of unsteady surface pressure measurements, dynamical characteristics of a laminar separation bubble subjected to forcing are extracted by online DMD. This method provides reliable updates of the modal characteristics of the separated flow as forcing is applied at a rate commensurate with the characteristic time scales of the flow. Therefore, online DMD applied to the surface pressure measurements provides a time-varying linear estimate of the nonlinear evolution of the controlled flow, thereby enabling closed-loop control. From this adaptive model, feedback control is implemented in which the Linear Quadratic Regulator gains are computed recursively as the model provided by online DMD is updated. The controller's explicit objective is to reduce the unsteady pressure fluctuations measured by surface mounted microphones within the separated flow region. Since this approach relies solely on observations of the separated flow, it is potentially robust to variable flow conditions. The chord Reynolds number of these experiments is 10^5 and the pulse-modulated zero-net mass-flux actuator slot is located just upstream of separation. It is found that applying adaptive feedback control using the LQR approach to determine the feedback gains results in slightly better flow reattachment (2% lower separation height) with a 5% reduction in actuator effort as compared with the best open loop forcing case. This approach does not require prior knowledge of the characteristics of the separated flow.

I. Introduction

A common goal of active flow control is to drive the dynamics of a particular fluid flow process to a more favorable condition with as little external effort as possible. This is often achieved by leveraging the inherent aerodynamic instabilities and allowing small inputs to be amplified to significantly impact the flow. Active flow control can be employed to alter aerodynamic forces over a body to increase lift and reduce drag, enhance mixing for efficient combustion processes, or target flow instabilities for aeroacoustic attenuation.

Boundary layer separation is at the heart of many detrimental conditions in aerodynamics. The increased pressure drag, loss of lift, and enhanced oscillatory loads due to flow separation can result in unfavorable conditions over a wing of an aircraft or blade elements in turbomachinery. Therefore, active flow control methods have been employed to delay, reduce, or reattach separated flow. The underlying dynamics of boundary layer separation are characterized by as many as three separate physical processes, which include the shear layer vortex amplification and convection due to the Kelvin-Helmholtz instability, wake dynamics, and separation bubble oscillations [1]. Depending upon the flow conditions, the frequencies associated with these processes may exhibit nonlinear lock-on [2].

*Ph.D. student and AIAA Member

[†]Professor and AIAA Associate Fellow

[‡]Graduate Student and AIAA Member

[§]Assistant Professor and AIAA Senior Member

[¶]Ph.D. student and AIAA Member

^{||}Professor and AIAA Associate Fellow

Regarding efficient separation control design and implementation, many parametric studies have been conducted in which actuation parameters are varied, and the performance is evaluated a posteriori [3–7]. Oscillatory actuation frequency was introduced as an important control parameter when Seifert et al. showed that control authority is potentially increased when an unsteady component is introduced [8]. Several studies aimed at determining the appropriate forcing frequency suggest forcing at the most amplified shear layer instability frequency results in flow separation mitigation [9–12]. However, this is not likely a universal optimal forcing frequency since Raju et al. show that the ideal forcing frequency varies with respect to actuator placement relative to the separation point [7].

Furthermore, the very goal of reducing the extent of a separation bubble by unsteady actuation suggests that the base state of the separated flow will undergo nonlinear deformation which will alter the preferred frequencies of the flow. Therefore, the optimal forcing frequency may vary as the base state is deformed. This is supported by the work by Marxen et al. in which the authors provide evidence that the optimal frequency is near the most amplified frequency of the controlled flow (as opposed to that of the uncontrolled flow) as identified by linear stability analysis [12]. This provides motivation for adaptive closed-loop separation control in which the dynamical model of the separated flow is updated as actuation is applied.

Moving to closed-loop separation control introduces additional complexity related to dynamical model derivation, objective function specification, and state measurement and estimation. The study by Tian et al. employ a downhill simplex approach to estimate the optimal control parameters for maximizing the lift to drag ratio for an experimental airfoil [13]. In this experiment, the aerodynamic forces acting on the airfoil were provided to the controller by a load cell. Additionally, Reese et al. use a neural network for adaptive system identification and control with the goal of maximizing lift over an airfoil estimated by a limited number of pressure sensors [14]. While these approaches were effective, they respond and adapt on timescales of the integrated aerodynamic forces. Also, for better or worse, these are model-free or black box approaches that largely neglect the underlying flow physics. Another approach for closed-loop separation control is developing a reduced-order model of the high-dimensional nonlinear dynamics. One such method is the Galerkin projection [15]. This is physics based, but the reduced-order model will likely not be valid if the base state deviates significantly due to forcing. Therefore, our objective is to provide an adaptive reduced-order model of the separated flow with reaction times that are on the order of the fluid dynamic (as opposed to the integrated forces) time scales that retains the essential physics of the separated flow.

Previous work shows that dynamic mode decomposition (DMD) serves to faithfully represent the stable limit cycle characteristics of a separated flow [16, 17]. In particular, the same traveling wave behavior of the shear layer vortex rollup and convection is captured by DMD derived from either the velocity or pressure fields, or unsteady surface pressure data [17]. In order to leverage this capability in an adaptive, closed-loop control setting, online DMD [18] will be employed to provide real-time dynamical system estimates of the separated flow that will be updated as forcing is applied. The measurements used to identify the discrete linear model provided by online DMD are unsteady surface pressure snapshots taken by a linear array of surface mounted microphones.

An adaptive closed-loop control approach is implemented that consists of feedback control for unsteady surface pressure suppression by rapidly updating feedback gains from a linear quadratic regulator (LQR) process. The response of the flow to control is measured by time-resolved PIV and fluctuating surface pressure measurements. Since this approach adapts to the measured data and does not require a priori information regarding the dynamics of the separated flow, this approach should be robust to a wide range of flow conditions.

II. Experimental Setup

This experimental study utilizes the canonical separated flow configuration described in [17, 19, 20] to remove pressure gradient dependencies on airfoil curvature. Laminar boundary layer separation occurs over a flat plate model due to an adverse pressure gradient imposed by siphoning a portion of the freestream flow through the ceiling of the wind tunnel test section and reinjecting it further downstream. This section provides details regarding the experimental design, data collection, real-time system, and the methods used for processing and analyzing the results.

A. Wind Tunnel Facility and Experimental Model

The Florida State Flow Control (FSFC) open-return wind tunnel facility housed the experiments for this study. The FSFC wind tunnel has a 9:1 inlet contraction and a test section of 30.5 cm in height and width, and 61.0 cm in length. Upstream of the contraction, anti-turbulence conditioning is accomplished by a honeycomb mesh and two screens. The freestream turbulence intensity integrated above 4 Hz at this flow speed is $u'/U_\infty = 0.5\%$. The flat plate model used in this study spans the entire width of the test section, has a chord dimension of $c = 40.2$ cm and thickness of $w = 0.095c$.

The leading edge of the plate is a 4:1 ellipse, and the trailing edge is square. A Pitot-static probe mounted upstream of the model monitors the freestream velocity, which is set to $U_\infty = 3.9$ m/s to provide a chord Reynolds number of $Re_c = 10^5$. The value from the Pitot probe is fed to the wind tunnel drive computer, and a simple PID controller adjusts the wind tunnel fan frequency to minimize variations in the freestream velocity. A schematic of the plate with relevant dimensions is shown in Figure 1.

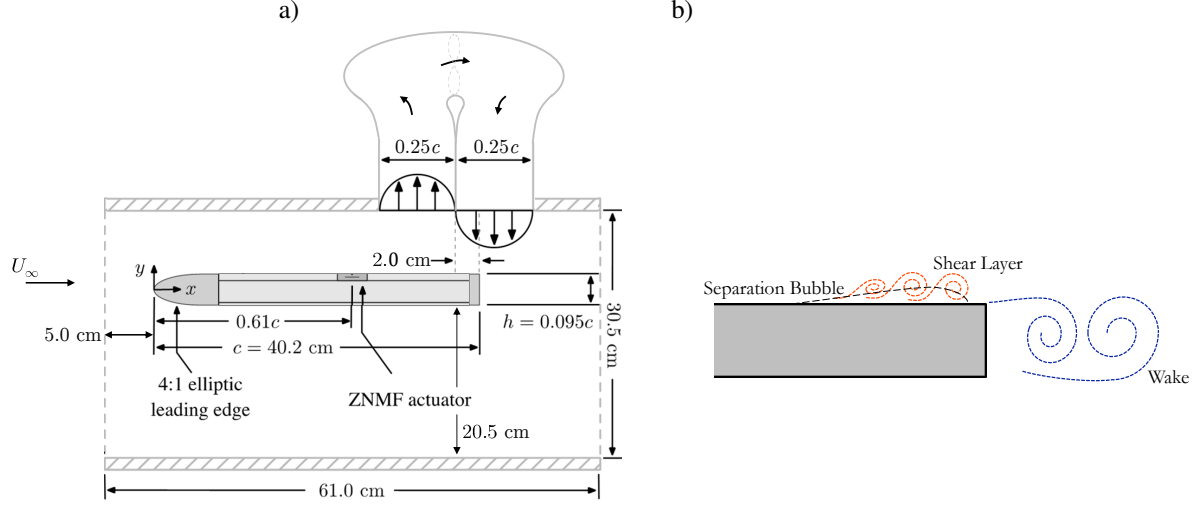


Fig. 1 a) Schematic of the flat plate model and flow separation system. b) Representation of the shear layer, separation bubble, and wake, which are active regions of the flow with coupled dynamics.

A suction/blowing boundary condition is imposed to enable boundary layer separation on the top surface of the flat plate. A DC motor driven fan pulls a portion of the freestream fluid through an acoustically treated perforated segment of the test section ceiling and then redirects the flow back into the test section through a similar return duct. The setup is designed to allow for the location and extent of the separation bubble to vary by changing the location of the plate with respect to the ceiling fan. For the current case, a closed separation bubble is generated that exhibits mean reattachment upstream of the trailing edge of the flat plate. The mean velocity profile upstream of the separation point is extracted from PIV snapshots, and the shape factor is estimated as $H = 2.67$ at $x/c \approx 0.3$. Comparing this to $H = 2.59$ for the Blasius boundary layer indicates that the flow is laminar upstream of separation.

B. Actuation

A rectangular slot zero-net mass-flux (ZNMF) actuator is employed to force the separated flow. The ZNMF jet sequentially ingests and expels surrounding fluid by varying the volume of a cavity underneath the slot. Thus, there is zero time-average mass flux but a non-zero momentum flux [21]. The actuator orifice is 2 mm wide, is located at $x/c = 0.61$, and spans the central 58% of the model. The actuator is comprised of four piezoelectric disks (APC Inc., PZT5J, Part Number: P412013T-JB) that serve to vary the volume of the cavity as unsteady voltages are applied across the disks.

The disks are driven by a high frequency sine wave, modulated down to the natural frequency range of the current separated flow. The frequency of the carrier sine wave is the $f_c = 2050$ Hz. The actuator output is expressed in terms of the momentum coefficient (c_μ), which is defined as

$$c_\mu = \frac{A_j v_{rms}^2}{A_{sep} U_\infty^2}. \quad (1)$$

In this definition, is the area of the actuator slot $A_j = W_j \times L_j$, and the separation area is the baseline length of the mean separation region multiplied by S , which is the span of the plate ($A_{sep} = L_{sep} \times S$). The RMS velocity of the jet is calculated from synchronized PIV measurements taken during control experiments.

C. Unsteady Pressure Sensors

The unsteady pressure on the model surface is measured by an array of 13 Panasonic WM-61A electret microphones. The diameter of the exposed microphone diaphragm of the WM-61A microphones is 2 mm, and the microphones are mounted mid-span in 8 mm increments from $x/c = 0.7$ to $x/c = 0.94$. The microphones are powered by a 4 mA constant current provided by an NI PXI-4498 data acquisition card. AC coupled, low-pass filters set to a cutoff frequency of 500 Hz condition and filter the microphone signal prior to analog-to-digital conversion. This cutoff frequency is set to ensure that the high frequency acoustic content from the actuator is sufficiently mitigated. Finally, the signals are digitized by an NI PXIe-6358 card for data acquisition and real-time control at a rate of 10 kHz.

For the microphone spectra presented here, the decontamination approach using conditioned spectral analysis described in [17, 22, 23] is employed. This effectively removes spurious signals captured by the microphones that are not due to separated flow hydrodynamics. In this case, reference microphones are mounted near the separation duct fan, and on the floor of the wind tunnel to identify contamination due to low frequency freestream unsteadiness and acoustics from the wind tunnel and separation duct drive fans. The contaminant signals are then conditioned to remove mutual coherence, then are used to remove the extraneous content from the surface mounted microphones.

D. Time-Resolved PIV

Both the separated flow region and actuator output are synchronously measured by Time-Resolved Particle Image Velocimetry (TR-PIV). The separation bubble measurement plane is oriented in the x - y plane, slightly offset from mid-span to reduce reflections from the surface mounted microphones. The light sheet grazes the top surface of the flat plate and the camera field of view has a streamwise extent of $x/c \approx 0.62$ to $x/c \approx 1$, and height of $y/c \approx 0.1$. Within the same plane, the actuator PIV region is bounded by $x/c \approx 0.59$ and $x/c \approx 0.63$, and has a height of $y/c = 0.087$. Olive oil droplets with nominal diameter of $1 \mu\text{m}$ introduced to the flow from a TSI 9307-6 atomizer are used for PIV seed particles[24]. The particles are illuminated by a high rep rate Nd-YAG laser operating in a single pulse configuration and images of the illuminated particles are acquired by a Phantom v1611 high speed camera. For the current sample rate, the resolution of the images is 1200×800 pixels and images are acquired at 10000 fps. In this case, the velocity vector fields are computed in between each image, so the effective PIV sample rate is 10000 Hz. Once images are acquired, image preprocessing and vector calculations are performed using LaVision DaVis 8.4.0 [25]. For the separated flow PIV measurement region, a multi-pass cross-correlation algorithm is used to determine the velocity vectors. The initial interrogation window size is 64×64 pixels and the final interrogation window size is 24×24 pixels with 75 % overlap. This results in a vector resolution of 0.729 mm per vector. The final window size of the higher magnification actuator measurement region is 48×48 pixels with 75 % overlap, which results in a vector resolution for these measurements of 0.266 mm per vector. The uncertainty in each vector field calculation is calculated using the correlation-statistics method for estimating PIV uncertainty [26]. The uncertainty of statistical quantities estimated by PIV snapshots is propagated from the snapshot uncertainties. A total of 4800 PIV vectors are acquired per acquisition sequence.

III. Dynamic Mode Decomposition

For the current study, variants of Dynamic Mode Decomposition (DMD) are employed for baseline flow analysis, and state space model identification for real-time control. Given many simultaneously sampled measurements of a particular dynamical process, DMD provides a discrete-time linear system that estimates the mapping of a current snapshot to the next snapshot in time [27–29].

The snapshot measurement vectors are denoted by italics as \mathbf{x}_k . The linear transition matrix provided by performing DMD on the set of measurements is labeled A_{DMD} , in which

$$\mathbf{x}_{k+1} = A_{DMD}\mathbf{x}_k. \quad (2)$$

Snapshot matrices are built from the individual snapshots vectors as

$$\mathbf{X} = \begin{bmatrix} | & | & & | \\ \mathbf{x}_1 & \mathbf{x}_2 & \cdots & \mathbf{x}_{n-1} \\ | & | & & | \end{bmatrix}, \quad \mathbf{Y} = \begin{bmatrix} | & | & & | \\ \mathbf{x}_2 & \mathbf{x}_3 & \cdots & \mathbf{x}_n \\ | & | & & | \end{bmatrix}. \quad (3)$$

The previous snapshot matrix is denoted by \mathbf{X} , and the current snapshot matrix (denoted by \mathbf{Y}) is the previous snapshot matrix shifted forward by one time step. Each snapshot vector consists of m simultaneous measurements, and a total of n snapshots are recorded. The snapshot matrices have dimension $m \times (n - 1)$.

The DMD transition matrix is then computed by multiplying the current snapshot matrix with the pseudoinverse (denoted by $^+$) of the previous snapshot matrix as [27]

$$A_{DMD} := \mathbf{Y}\mathbf{X}^+. \quad (4)$$

For no modal truncation, the number of DMD modes and eigenvalues will be $\min(m, n - 1)$. For the case in which it is expected that fewer states are required to capture the dynamics, a reduced problem can be formulated by taking the singular value decomposition (SVD) of the snapshot matrix $\mathbf{X} = \mathbf{U}\mathbf{\Sigma}\mathbf{V}^*$, in which * denotes the complex conjugate transpose. This result is substituted into (4) to yield

$$A_{DMD} = \mathbf{Y}[\mathbf{U}\mathbf{\Sigma}\mathbf{V}^*]^+ = \mathbf{Y}\mathbf{V}\mathbf{\Sigma}^+\mathbf{U}^*. \quad (5)$$

The dimensional reduction is performed by truncating the SVD of \mathbf{X} to include only the first r singular values, in which a subscript r will denote a truncated matrix. From this, the reduced proxy system matrix can be determined by

$$\tilde{A} = \mathbf{U}_r^* A_{DMD} \mathbf{U}_r = \mathbf{U}_r^* \mathbf{Y} \mathbf{V}_r \mathbf{\Sigma}_r^+. \quad (6)$$

The DMD results presented in this study from PIV measurements are computed using the Total Least Squares DMD algorithm presented in Hemati et al. This consists of a preprocessing step that serves to remove the asymmetric treatment of measurement noise inherent in the formulation of DMD provided above. [16]

A. Online DMD

The DMD formulation provided above requires that every snapshot of \mathbf{X} be readily available to be manipulated in a computer's RAM to compute the SVD. This allows for the a posteriori dynamical analysis of a measurement ensemble from a linear system perspective. However, for the current case, the separated flow can experience significant deviations in its dynamics as forcing is applied. Therefore, the transition matrix identified by DMD for the baseline separated flow case will not be valid once actuation is implemented. Real-time tracking of the deviations in the separated flow dynamics will allow for more efficient control. This is accomplished by Online DMD using an array of surface pressure measurements [17, 18].

Online DMD provides an updated DMD matrix as soon as a new snapshot becomes available. Therefore, the variations in the dynamics are represented as a time varying linear system. As long as the size of the snapshot is not too large, this update step can be done at a rate that is faster than the characteristic frequencies of the flow. This rapidly adapting linear system representation of the separated flow can then be used to estimate future states for control.

Beginning with the definition of the DMD transition matrix (4), and the property of the pseudoinverse, $\mathbf{X}^+ = \mathbf{X}^T [\mathbf{X}\mathbf{X}^T]^{-1}$ the formulation of online DMD begins with defining two new matrices, \mathbf{Q} and \mathbf{P} ,

$$\mathbf{A} = \mathbf{Y}\mathbf{X}^+ = \mathbf{Y}\mathbf{X}^T [\mathbf{X}\mathbf{X}^T]^{-1} = \mathbf{Q}\mathbf{P}. \quad (7)$$

The new matrices are defined as, $\mathbf{Q} := \mathbf{Y}\mathbf{X}^T$ and $\mathbf{P} := [\mathbf{X}\mathbf{X}^T]^{-1}$. If a new snapshot $(\mathbf{x}_{k+1}, \mathbf{y}_{k+1})$ is to be included in the snapshot matrix, \mathbf{Q} and \mathbf{P} can be appended as

$$\begin{aligned} \mathbf{Q}_{k+1} &= [\mathbf{Y} \ \mathbf{y}_{k+1}][\mathbf{X} \ \mathbf{x}_{k+1}]^T = \mathbf{Q} + \mathbf{y}_{k+1} \mathbf{x}_{k+1}^T, \text{ and} \\ \mathbf{P}_{k+1} &= ([\mathbf{X} \ \mathbf{x}_{k+1}][\mathbf{X} \ \mathbf{x}_{k+1}]^T)^{-1} = [\mathbf{P}^{-1} + \mathbf{x}_{k+1} \mathbf{x}_{k+1}^T]^{-1}. \end{aligned}$$

The expression for \mathbf{P}_{k+1} is in a form that can be computed by the Sherman-Morrison formula,

$$\mathbf{P}_{k+1} = [\mathbf{P}^{-1} + \mathbf{x}_{k+1} \mathbf{x}_{k+1}^T]^{-1} = \mathbf{P} - \gamma \mathbf{P} \mathbf{x}_{k+1} \mathbf{x}_{k+1}^T \mathbf{P}. \quad (8)$$

The scalar, γ is defined as $\gamma := 1/(1 + \mathbf{x}_{k+1}^T \mathbf{P} \mathbf{x}_{k+1})$. Therefore, given current estimates of \mathbf{Q} and \mathbf{P} , the DMD transition matrix is updated for each new snapshot by $\mathbf{A}_{k+1} = \mathbf{Q}_{k+1} \mathbf{P}_{k+1}$, after some substitution (see Zhang et al. [18]),

$$\mathbf{A}_{k+1} = \mathbf{A} + \gamma(\mathbf{y}_{k+1} - \mathbf{A}\mathbf{x}_{k+1})\mathbf{x}_{k+1}^T \mathbf{P}. \quad (9)$$

For the initial case in which there is no current estimate for \mathbf{A} and \mathbf{P} , \mathbf{A}_0 can be initialized randomly, and $\mathbf{P}_0 = \alpha \mathbf{I}$ such that the parameter α is very large so $\mathbf{P}_0^{-1} \approx \mathbf{0}$.

In order to discard the contribution previous snapshots have on the current DMD estimate, a weighting factor is defined to smoothly diminish old snapshots. Resulting in refreshed dynamical estimates from online DMD. The weighting factor acts on an ensemble of snapshot vectors as so:

$$\boldsymbol{\chi} = \begin{bmatrix} | & | & & | \\ (\sqrt{\kappa})^{n-1} \mathbf{x}_1 & (\sqrt{\kappa})^{n-2} \mathbf{x}_2 & \cdots & \mathbf{x}_{n-1} \\ | & | & & | \end{bmatrix}, \quad \boldsymbol{\psi} = \begin{bmatrix} | & | & & | \\ (\sqrt{\kappa})^{n-1} \mathbf{x}_2 & (\sqrt{\kappa})^{n-2} \mathbf{x}_3 & \cdots & \mathbf{x}_n \\ | & | & & | \end{bmatrix}.$$

Setting the weighting factor low ($\kappa \rightarrow 0$) aggressively attenuates old snapshots, while setting the weighting factor close to one ($\kappa \rightarrow 1$) allows the old snapshots to gradually decay. These weighted snapshot matrices are substituted into the definition of DMD $\mathbf{A}_W = \boldsymbol{\psi} \boldsymbol{\chi}^+$, and online DMD is carried out as before [18]. The end result is that the weighting factor penalizes the updated value of \mathbf{P}_{k+1} as so,

$$\mathbf{P}_{k+1} = \frac{1}{\kappa} (\mathbf{P} - \gamma \mathbf{P} \boldsymbol{\chi} \mathbf{x}_{k+1} \mathbf{x}_{k+1}^T \mathbf{P}). \quad (10)$$

This approach is useful for real-time DMD estimates as long as the computational effort required to update the DMD estimates remains low. Online DMD requires $\mathcal{O}(m^2)$ operations in updating the DMD estimates. [18] Thus, this algorithm is well suited to the low-dimensional surface pressure measurements, in contrast to streaming DMD which is beneficial for high-dimensional data [30]. More information regarding the relative time required for various DMD algorithms is provided in Zhang et al. [18] It should be noted that this approach is formulated for cases in which there is no external forcing. However online DMD can also be implemented for control cases by appending the DMD matrix as shown in [17, 31].

IV. Closed Loop Separation Control Approach

Since online DMD provides a linear representation of the evolution of the surface pressure fluctuations, classical linear control methods may be viable for autonomous feedback control. For example, if the objective is to suppress the pressure fluctuations, the control input can be defined as a state feedback $\mathbf{u}_k = -\mathbf{K}\mathbf{x}_k$, and the linearization provided by online DMD can be expressed as

$$\mathbf{x}_{k+1} = (\mathbf{A} - \mathbf{B}\mathbf{K})\mathbf{x}_k, \quad (11)$$

in which \mathbf{A} is the current discrete linear state dynamics and \mathbf{B} is the current actuation mapping matrix identified by online DMD. At this point, the Linear Quadratic Regulator (LQR) method can be used to determine \mathbf{K} for the current system estimate with respect to a weighting term applied to the state space and the actuator effort. As the flow is forced, the linear estimation will vary. Therefore, the \mathbf{K} matrix will need to be updated periodically. In general, this feedback term will not provide optimal control since the underlying dynamics are not linear and time invariant. However, this is the set of optimal feedback gains for the current dynamical estimate provided by online DMD.

Using the discrete linear system representation provided by online DMD, LQR controller feedback gains are computed and updated periodically. These feedback gains are then employed to attenuate the unsteady pressure fluctuations within the separated flow region. The control signal is defined as a negative feedback $\mathbf{u}_k = -\mathbf{K}_{lqr}\mathbf{x}_k$, in which \mathbf{K}_{lqr} is determined by minimizing the cost function

$$J = \sum_{k=0}^{\infty} \left(\mathbf{x}_k^T \mathbf{Q}_{lqr} \mathbf{x}_k + \mathbf{u}_k^T \mathbf{R}_{lqr} \mathbf{u}_k \right). \quad (12)$$

See Dorf & Bishop [32] for details. The appropriate choice of \mathbf{Q}_{lqr} and \mathbf{R}_{lqr} balances the state space reference error and the actuator input. The solution for \mathbf{K}_{lqr} is

$$\mathbf{K}_{lqr} = (\mathbf{R}_{lqr} + \mathbf{B}^T \mathbf{P}_R \mathbf{B})^{-1} \mathbf{B}^T \mathbf{P}_R \mathbf{A}, \quad (13)$$

in which, P_R is determined from the discrete-time Riccati equation,

$$P_R = A^T P_R A - (A^T P_R B)(B^T P_R B + R_{lqr})^{-1}(A^T P_R B)^T + Q_{lqr}. \quad (14)$$

This process is implemented using the LabVIEW linear quadratic regulator VI from the control design and simulation module. [33]

V. Analysis of the Baseline Separated Flow

This section provides baseline separated flow characteristics beginning with estimates of the spectral content of the flow from surface pressure measurements. Then, attention is turned to full-field flow evaluation from PIV measurements. The results of controlling the separated flow will be compared with these baseline characteristics.

A. Unsteady Pressure

The unsteady pressure fluctuations within the separated flow are recorded by microphones that lie within the mean recirculation region. Premultiplied PSD estimates for these measurements are plotted with respect to Strouhal number in Figure 2. The Strouhal number is defined as

$$St_{L_{sep}} = fL_{sep}/U_\infty. \quad (15)$$

For the plots shown, a total of 30 seconds of data acquired at 10 kHz are used to estimate the PSD. The number of samples used per ensemble is 10,000 resulting in $\Delta f = 1$ Hz. The ensembles are scaled by a Hann window and are overlapped by 75%.

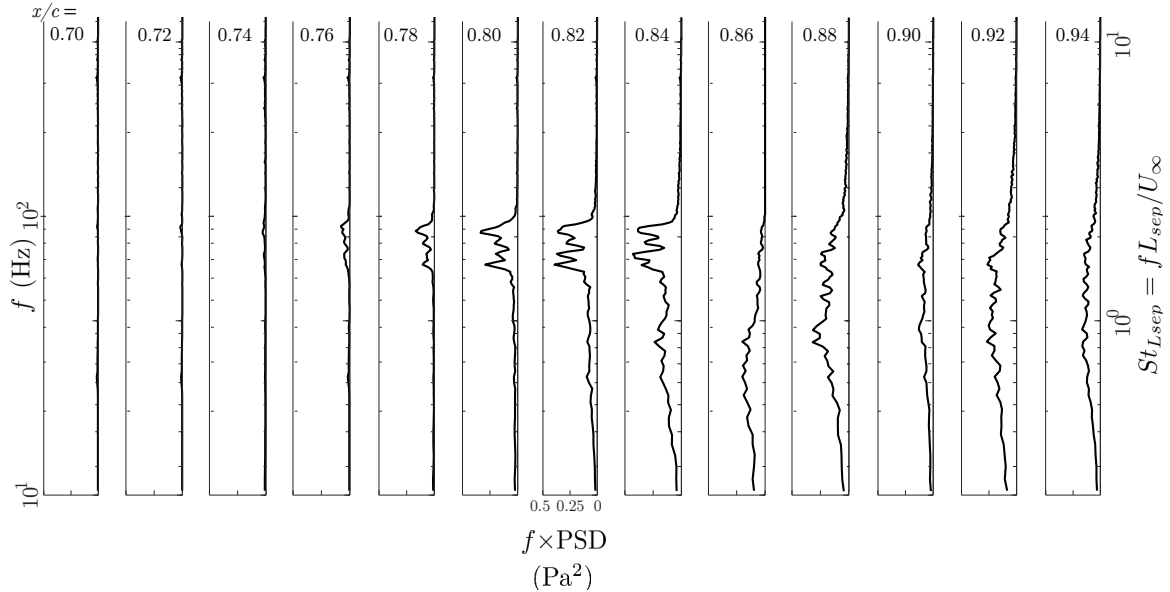


Fig. 2 Premultiplied power spectral density plots of the corrected surface mounted microphone array measurements after the contaminating signals have been removed. The microphone location for each plot is denoted at the top of the plot.

The corrected, premultiplied power spectral density plots for the microphone array are provided with fixed axis limits to show the streamwise development of the oscillatory content in Figure 2. This shows the spatial evolution of the Kelvin-Helmholtz instability into an active frequency range between $St_{L_{sep}} = 1.50$ and 2.30 . This content begins to decay near the mean reattachment region as the flow transitions to turbulent flow, and spectral broadening occurs.

B. PIV

PIV snapshots provide spatially resolved mean and turbulent quantities of the baseline flow. Since a high speed PIV system is utilized, the sample rate of the velocity snapshots is much higher than the characteristic frequencies of the

flow. Thus, frequency spectrum estimates can be extracted from the flow field data by Fourier analysis or DMD. The TR-PIV dataset for the uncontrolled, canonical separated flow ($Re_c = 10^5$) studied here consists of at least $m = 4800$ snapshots, each with $n = 10\,032$ vectors per snapshot. Figure 3 contains vorticity contours of the mean of the PIV snapshots. The separation region is illustrated by the line of $\bar{u} = 0$, depicted as the black dashed line. The length of the mean separation bubble is found to be $L_{sep} = 0.24c$, and the height is $h_{sep} = 0.0171c$.

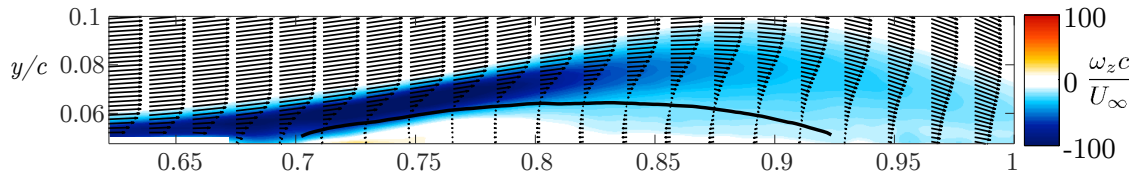


Fig. 3 Average z -vorticity as computed from PIV snapshots. The line of $\bar{u} = 0$ is the black line.

Total least squares DMD is applied to the TR-PIV snapshots of the baseline separated flow in order to identify global dynamical characteristics of the flow. Since power spectrum derived from surface pressure measurements and previous studies indicate that at least 3 oscillatory phenomena exist simultaneously in the baseline flow [1, 19], the DMD estimate can be rank-reduced. A rank-reduction level of $r = 25$ is used, which corresponds to retaining over 99% of the fluctuating kinetic energy content based on an SVD of \mathbf{X} . Figure 4 contains the DMD eigenvalues plotted on the complex plane alongside the modal oscillatory amplitude plotted with respect to Strouhal number. This plot shows that the dominant modes extracted via DMD are non-decaying and purely oscillatory (i.e., the eigenvalues lie very close to the unit circle). This is expected due to the oscillatory, stable limit cycle characteristics of the separated flow.

Additionally, the highest modal amplitude occurs at $St_{L_{sep}} = 2.01$. The PSD estimates of the unsteady pressure data provided in the previous section corroborates the existence of this frequency content. This DMD mode describes the most energetic component of the limit cycle of the baseline separated flow. In Figure 5, the real part of the DMD modes are visualized as vorticity contours. The spatial mode for $St_{L_{sep}} = 2.01$ is composed of patterned, coherent vorticity structures. As shown in Deem et al. [17], this mode exhibits traveling wave characteristics.

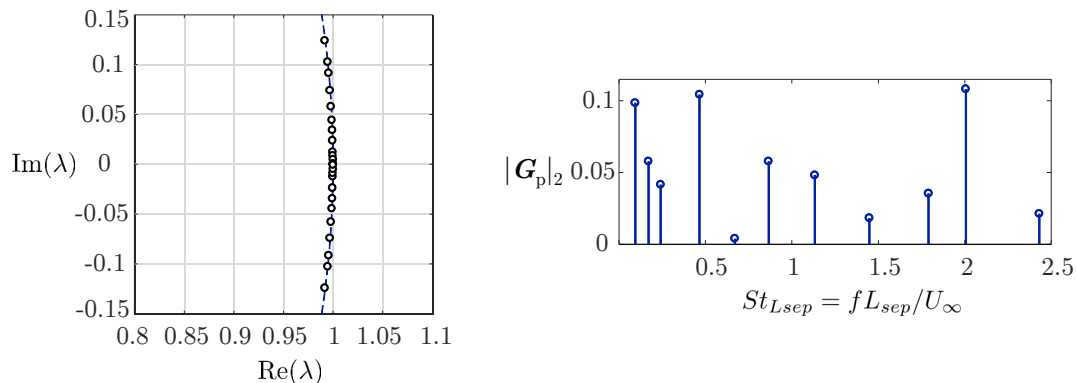


Fig. 4 a) DMD eigenvalues plotted on the complex plain. b) 2-norm of the DMD oscillatory amplitude plotted with respect to $St_{L_{sep}}$.

VI. Separated Flow response to Periodic Forcing

The response of the separated flow subjected to periodic forcing is measured by PIV. Two momentum coefficients are tested for a range of actuation frequencies. The momentum coefficient is determined by computing the RMS velocity as measured by PIV at the midline of the actuator, at a height of approximately 0.4 mm above the actuator slot. A

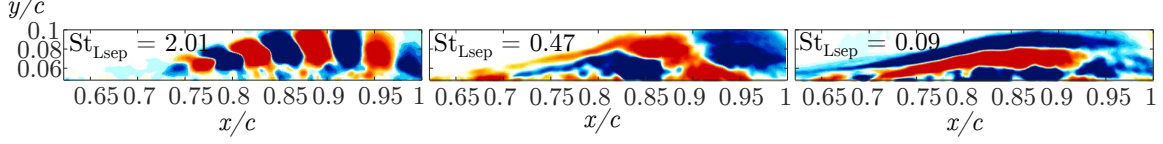


Fig. 5 Real part of the vorticity of the DMD modes corresponding to the three highest amplitude modes identified by TDMD.

burst modulated waveform is used for these cases, in which the carrier frequency (f_c) sine wave is cycled on and off impulsively at the burst frequency f_b . The nominal duty cycle of the modulation is set to 50%. However, in order to prevent spectral leakage and unanticipated high-frequency content, the duty cycle can vary from this slightly to ensure that an integer number of carrier cycles exists within the burst period. The forcing frequency is nondimensionalized with respect to the separation bubble length and freestream velocity as

$$F^+ = \frac{f_b L_{sep}}{U_\infty}. \quad (16)$$

An illustration of the burst modulation waveform is provided in Figure 6.

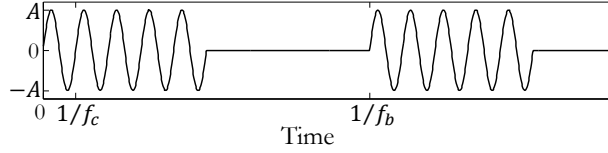


Fig. 6 Burst modulation waveform used for periodic actuation.

The forcing frequencies tested in this case span from $F^+ = 0.98$ to 4.61 and the momentum coefficients tested are $C_\mu = 3.8 \times 10^{-4}$ and $C_\mu = 5.7 \times 10^{-4}$. As a performance metric, the height of the mean reversed flow region is determined from PIV measurements for each forcing frequency (i.e., an indication for the size of the separation bubble) and plotted in Figure 7.

Although flow separation is reduced over a broad range ($F^+ \approx 1$ to 2.5), forcing at $F^+ \approx 2$ exhibits the best performance for both actuation amplitudes. This frequency corresponds to the dominant modal amplitude identified by DMD. This corroborates the results of prior literature which show that targeting the natural dynamics of separated flow is an effective strategy for reducing separation [7, 11, 12, 19, 20].

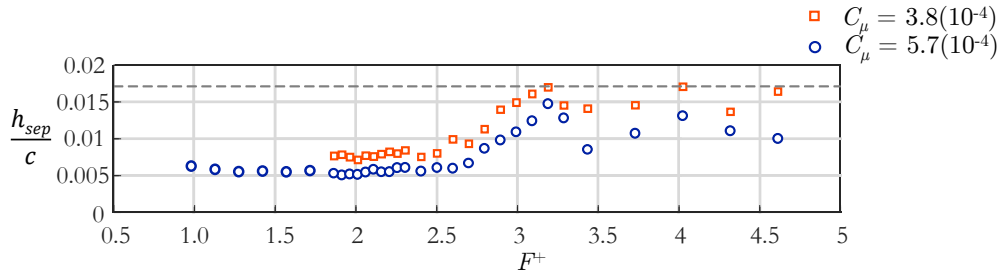


Fig. 7 Normalized mean separation height plotted against input frequency. The minimum mean separation height measured corresponds to forcing at the dominant frequency identified by DMD, $F^+ \approx 2$. The baseline separation height of $h_{sep}/c = 0.0171$ is denoted by the dashed gray line.

VII. Adaptive Closed Loop Control of Separated Flow

The unsteady pressure within the separated flow region is provided by the surface mounted microphone array to a real-time implementation of online DMD in order to estimate a linear model of the dynamical system responsible for the

separated flow state evolution. This time varying, adaptive linear model is used in the control approaches described below. Each element of the control loop is coded in either Simulink or LabView and compiled with NI Veristand 2017 [33]. The code is then deployed to an NI PXIe-8880 real-time controller for state measurement, online model estimation, feedback gain calculation, and actuation signal generation.

Prior to being digitized, the microphone signals are filtered and ac-coupled by external variable frequency low pass filters with a cut-off frequency of 500 Hz. The data acquisition rate is set to be 10 kHz for all control methods. For ZNMF actuation, the input waveform is multiplied by the carrier sine wave, amplified by an external amplifier, then sent to the actuator.

A. LQR Control

With the goal of reducing the surface pressure fluctuations, a negative feedback controller is implemented by recursively computing LQR gains. As actuation is provided, and online DMD updates the linear estimation with each new pressure snapshot and actuator input sample.

The nominal loop rate of the pressure snapshot acquisition, online DMD estimation, and input signal calculation is 10 kHz, which is more than 100 times faster than the dominant frequency of the separated flow. Due to the computational expense of solving the Riccati equation, the LQR feedback gains are updated every 30 primary loop cycles. This results in updating the feedback gains at a rate of 333.33 Hz. The LQR weights are set to be $\mathbf{Q}_{lqr} = 20 \times \mathbf{I}$ and $\mathbf{R}_{lqr} = 0.3$, which allowed the actuator effort to be maximized at the saturation limit. The online DMD weighting factor is set to 0.99995, which results in previous snapshot attenuation of 50% after 2.77 seconds. If time is nondimensionalized with respect to the dominant DMD mode frequency ($f_{SL} \approx 82$ Hz), 50% snapshot attenuation occurs after $\tau = 227$ characteristic periods.

PIV measurements are taken to quantify the response of the adaptive LQR control on the separated flow. The mean of 4800 PIV snapshots is provided in Figure 8. The recirculation region is significantly reduced, with a mean separation height of $h_{sep}/c = 0.0052$. The momentum coefficient is estimated from the PIV measurements as $C_\mu = 5.4 \times 10^{-4}$. This results in slightly better performance (within the uncertainty) than the best open loop results, with a 5% reduction in actuation effort. Furthermore, this is accomplished without any prior knowledge of the characteristics of the separated flow.

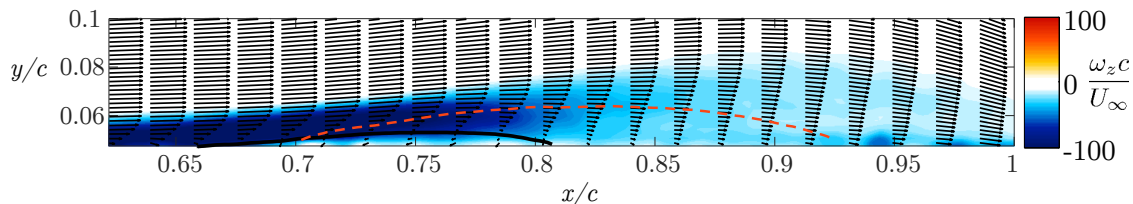


Fig. 8 Average z -vorticity for separated flow subjected to adaptive LQR control as computed from 4800 PIV snapshots. The recirculation region is denoted by line of $\bar{u} = 0$ depicted by the solid black line. For reference, the recirculation region of the baseline separated flow is shown as the dashed orange line. This shows that applying the adaptive feedback control using LQR gains significantly reduces the size of the separation region.

Due to the unsteady nature of this adaptive control approach, the control input will vary as the separated flow deforms under actuation and the model is updated. Variations in the input signal are visualized as a power spectrogram, shown in Figure 9. Each input ensemble is scaled by a Hann window prior to computing the spectral estimates. The frequency resolution of the power spectrum is $\Delta f = 1$ Hz, the total length for each power spectral density estimate is 10000 samples, and a new PSD is evaluated every 0.1 seconds (1000 samples). The time is nondimensionalized with respect to the shear layer frequency identified by DMD of the baseline flow ($f_{SL} \approx 82$ Hz). From the spectrogram, as soon as the control is turned on, the input spectra contains primarily low frequency content, with some broadband fluctuations. The actuation signal then settles to $St_{Lsep} \approx 1.8$ after 100 shear layer periods, after which it seems to prefer lower frequencies while varying between $St_{Lsep} = 1$ and 2.

To visualize the transient response of the flow to LQR control, PIV acquisition was triggered by the initialization of the controller, and the mean of 300 PIV snapshots is computed for every 10 samples. The separation height is determined from each mean field, and is plotted in Figure 10. A distinct dip in separation height is observed at $\tau = 5$, indicating that the control effectively reduces the separation region after only 5 shear layer periods.

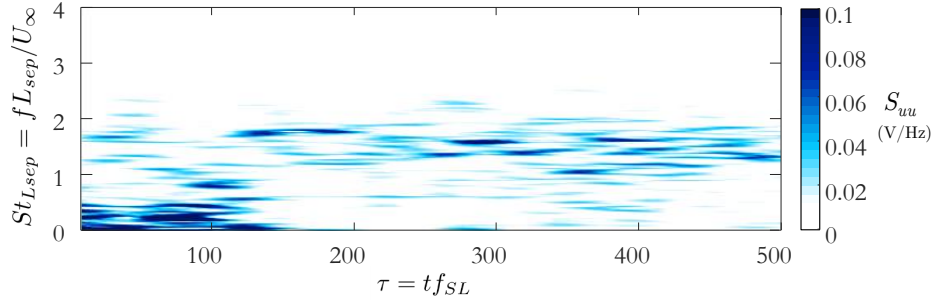


Fig. 9 The frequency content of the actuation signal plotted with respect to shear layer periods as a spectrogram. This shows that the input signal exhibits unsteady frequency content and takes on multiple frequencies simultaneously.

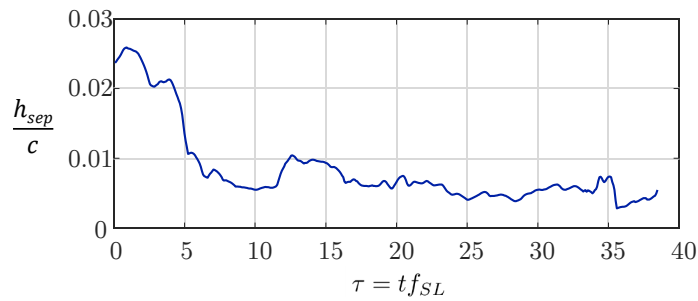


Fig. 10 A running calculation of the mean separation height to illustrate the transient response of the flow to adaptive LQR-gain feedback control. This is computed by taking the mean separation height of 300 PIV snapshots, every $\tau = 0.082$.

VIII. Conclusions

Real-time, adaptive control is implemented to reattach separated flow in an autonomous manner. Measurements of unsteady surface pressure are used to determine a linear model of the flow that is allowed to update with each new measurement. This allows the estimate of the dynamical system to update in real-time as forcing is applied and new flow modes are excited or nonlinear deviations occur. This adaptive dynamical estimate enables the use of linear closed-loop control techniques to efficiently reattach the separated flow.

To provide a repeatable separated flow that is not dependent upon specific airfoil curvature, an adverse pressure gradient is induced over a flat plate model, which in turn separates a laminar boundary layer from the surface of the model. The flow is forced by a 2-D ZNMF jet in which the output is monitored by PIV both near the jet exit, and within the separated flow region. By measuring the response of the flow to periodic forcing, it is found that the flow exhibits the most reattachment when the modulation frequency is near that of the frequency of the shear layer DMD mode.

Negative feedback control is then implemented in which LQR gains are recursively computed as the model estimates change. Since this is not a linear time invariant system, this is not optimal control *per se*, though it does provide the optimal control gains for the current linear time invariant system estimate. PIV measurements taken during this experiment show that the mean separation region for this control case is significantly reduced. The resulting mean separation height for this control approach is slightly less than the best open-loop control case, with an observed reduction in actuator momentum coefficient by 5%. Due to the quickly adapting model and feedback gain calculation, this control approach allows for rapid flow reattachment. Only five characteristic time units are required for the flow to exhibit reattachment.

Since this approach does not require any prior information regarding the dynamical characteristics of the flow, this approach should be robust to varying flow conditions. Future work will entail testing the robustness of this control approach by altering the Reynolds number and the separation bubble height, inducing time dependent variations in the imposed adverse pressure gradient, and enforcing turbulent separation. These variations along with variations in the penalty terms in determining the feedback gains will be tested.

IX. Acknowledgments

Funding for this work is provided under AFOSR Grant FA9550-14-1-0289 and AFOSR Grant FA9550-17-1-0252, monitored by Dr. Doug Smith.

References

- [1] Mittal, R., Kotapati, R. B., and Cattafesta, L., “Numerical study of resonant interactions and flow control in a canonical separated flow,” *AIAA paper*, Vol. 1261, 2005, p. 1261.
- [2] Kotapati, R. B., Mittal, R., Marxen, O., Ham, F., You, D., and Cattafesta, L. N., “Nonlinear dynamics and synthetic-jet-based control of a canonical separated flow,” *Journal of Fluid Mechanics*, Vol. 654, 2010, pp. 65–97.
- [3] Seifert, A., Darabi, A., and Wyganski, I., “Delay of airfoil stall by periodic excitation,” Vol. 33, 1996, pp. 691–698.
- [4] Seifert, A., and Pack, L. G., “Oscillatory Control of Separation at High Reynolds Numbers,” *AIAA Journal*, Vol. 37, 1999, pp. 1062–1071. doi:10.2514/2.834.
- [5] Glezer, A., Amitay, M., and Honohan, A. M., “Aspects of low-and high-frequency actuation for aerodynamic flow control,” *AIAA journal*, Vol. 43, No. 7, 2005, p. 1501.
- [6] Mittal, R., and Kotapati, R. B., “Resonant mode interaction in a canonical separated flow,” *IUTAM Symposium on Laminar-Turbulent Transition*, Springer, 2006, pp. 341–348.
- [7] Raju, R., Mittal, R., and Cattafesta, L., “Dynamics of airfoil separation control using zero-net mass-flux forcing,” *AIAA journal*, Vol. 46, No. 12, 2008, p. 3103.
- [8] Seifert, A., Bachar, T., Koss, D., Shepshelovich, M., and Wygnanski, I., “Oscillatory blowing: a tool to delay boundary-layer separation,” *AIAA journal*, Vol. 31, No. 11, 1993, pp. 2052–2060.
- [9] Yarusevych, S., Kawall, J., and Sullivan, P. E., “Airfoil performance at low Reynolds numbers in the presence of periodic disturbances,” *Journal of fluids engineering*, Vol. 128, No. 3, 2006, pp. 587–595.
- [10] Postl, D., Balzer, W., and Fasel, H., “Control of laminar separation using pulsed vortex generator jets: direct numerical simulations,” *Journal of Fluid Mechanics*, Vol. 676, 2011, pp. 81–109.
- [11] Yarusevych, S., and Kotsonis, M., “Steady and transient response of a laminar separation bubble to controlled disturbances,” *Journal of Fluid Mechanics*, Vol. 813, 2017, pp. 955–990.
- [12] Marxen, O., Kotapati, R. B., Mittal, R., and Zaki, T., “Stability analysis of separated flows subject to control by zero-net-mass-flux jet,” *Physics of Fluids*, Vol. 27, No. 2, 2015, p. 24107.
- [13] Cattafesta, L., Tian, Y., and Mittal, R., “Adaptive control of post-stall separated flow application to heavy vehicles,” *The Aerodynamics of Heavy Vehicles II: Trucks, Buses, and Trains*, 2009, pp. 151–160.
- [14] Reese, B. M., Collins Jr, E. G., Fernandez, E., and Alvi, F. S., “Nonlinear Adaptive Approach to Microjet-Based Flow Separation Control,” *AIAA Journal*, 2016.
- [15] Noack, B. R., Morzynski, M., and Tadmor, G., *Reduced-order modelling for flow control*, Vol. 528, Springer Science & Business Media, 2011.
- [16] Hemati, M. S., Rowley, C. W., Deem, E. A., and Cattafesta, L. N., “De-biasing the dynamic mode decomposition for applied Koopman spectral analysis of noisy datasets,” *Theoretical and Computational Fluid Dynamics*, 2017, pp. 1–20.
- [17] Deem, E., Cattafesta, L., Zhang, H., Rowley, C., Hemati, M., Cadieux, F., and Mittal, R., “Identifying Dynamic Modes of Separated Flow Subject to ZNMF-based Control from Surface Pressure Measurements,” *47th AIAA Fluid Dynamics Conference*, 2017, p. 3309. AIAA Paper 2017-3309.
- [18] Zhang, H., Rowley, C. W., Deem, E. A., and Cattafesta, L. N., “Online dynamic mode decomposition for time-varying systems,” *arXiv preprint arXiv:1707.02876*, 2017.
- [19] Griffin, J., Oyarzun, M., Cattafesta, L. N., Tu, J. H., Rowley, C. W., and Mittal, R., “Control of a canonical separated flow,” *43rd Fluid Dynamics Conference*, 2013. AIAA Paper 2013-2968.

- [20] Hemati, M. S., Deem, E. A., Williams, M. O., Rowley, C. W., and Cattafesta, L. N., "Improving Separation Control with Noise-Robust Variants of Dynamic Mode Decomposition," *54th AIAA Aerospace Sciences Meeting*, 2016, p. 1103. AIAA Paper 2016-1103.
- [21] Holman, R., Utturkar, Y., Mittal, R., Smith, B. L., and Cattafesta, L., "Formation criterion for synthetic jets," *AIAA journal*, Vol. 43, No. 10, 2005, p. 2110.
- [22] Bendat, J. S., and Piersol, A. G., *Random data: analysis and measurement procedures*, Vol. 729, John Wiley & Sons, 2011.
- [23] Bendat, J. S., and Piersol, A. G., *Engineering applications of correlation and spectral analysis*, Wiley-Interscience, 2013. 315 p., 2013.
- [24] Melling, A., "Tracer particles and seeding for particle image velocimetry," *Measurement Science and Technology*, Vol. 8, No. 12, 1997, p. 1406.
- [25] "LaVision, DaVis v8.4.x," 2017.
- [26] Wieneke, B., "PIV uncertainty quantification from correlation statistics," *Measurement Science and Technology*, Vol. 26, No. 7, 2015, p. 74002.
- [27] Tu, J. H., Rowley, C. W., Luchtenburg, D. M., Brunton, S. L., and Kutz, J. N., "On Dynamic Mode Decomposition: Theory and Applications," *Journal of Computational Dynamics*, Vol. 1, No. 2, 2014, pp. 391–421.
- [28] Schmid, P. J., "Dynamic mode decomposition of numerical and experimental data," *Journal of fluid mechanics*, Vol. 656, 2010, pp. 5–28.
- [29] Rowley, C. W., Mezić, I., Bagheri, S., Schlatter, P., and Henningson, D. S., "Spectral analysis of nonlinear flows," *Journal of fluid mechanics*, Vol. 641, 2009, pp. 115–127.
- [30] Hemati, M. S., Williams, M. O., and Rowley, C. W., "Dynamic mode decomposition for large and streaming datasets," *Physics of Fluids*, Vol. 26, No. 11, 2014, p. 111701.
- [31] Proctor, J. L., Brunton, S. L., and Kutz, J. N., "Dynamic mode decomposition with control," *SIAM Journal on Applied Dynamical Systems*, Vol. 15, No. 1, 2016, pp. 142–161.
- [32] Dorf, R. C., and Bishop, R. H., *Modern control systems*, Pearson, 2011.
- [33] "National Instruments, NI VeriStand 2017," 2017.